Nanoscale Advances

ROYAL SOCIETY OF CHEMISTRY

PAPER

View Article Online
View Journal | View Issue

Cite this: *Nanoscale Adv.*, 2026, **8**, 167

Exploring a GE/Nafion/Co-MOF nanosheets/CuO NPs/GOx powered electrochemical biosensor for ultrasensitive detection of rebaudioside A

Manju Manuel, [ab] Suvardhan Kanchi *[ab] and Venkatramana Losetty [c]

Rebaudioside A (Reb A) is a natural, non-nutritive sweetener highly prevalent in the global sweetener market and widely preferred by consumers. In this study, an advanced electrochemical biosensor was developed for sensing Reb A, using a modified graphite rod electrode extracted from discharged Zn–C batteries. The electrode was fabricated using a layer-by-layer strategy with Nafion, Co-MOF nanosheets, CuO NPs, and glucose oxidase (GOx) enzyme. The nanomaterials were characterized by UV-vis, FTIR, DLS, zeta potential measurements, XRD, Raman, SEM, TEM, EDS, and XPS techniques. Electrochemical characterization *via* Cyclic Voltammetry (CV) and Electrochemical Impedance Spectroscopy (EIS) revealed a significant enhancement in electrical conductivity and increased electroactive surface area. The designed biosensor exhibited a sharp oxidation peak at 0.16 V due to ester bond cleavage in Reb A, which was further amplified in the presence of GOx, resulting from hydroxyl oxidation and hydrogen peroxide generation. Differential pulse voltammetry (DPV) demonstrated a linear response over a concentration range of 2.0–14 μM (R^2 = 0.993) with a limit of detection (LOD) of 0.23 μM. The sensor displayed excellent analytical performance, with repeatability, reproducibility (RSD = 3.9%), and stability. Additionally, recovery studies confirmed its accuracy, ranging from 97% to 98.17%. Further, the molecular docking studies confirmed strong Reb A–GOx interactions (−7.26 kcal mol^{-1}), supporting the biosensor's specificity. The developed biosensor demonstrates excellent analytical performance, making it highly suitable for routine laboratory analysis of sweeteners in complex food matrices.

Received 16th June 2025
Accepted 7th September 2025

DOI: 10.1039/d5na00591d

rsc.li/nanoscale-advances

1. Introduction

Natural sweeteners have emerged as significant alternatives to artificial sweeteners in the global food industry due to their low caloric content and potential health benefits.[1] Steviol glycosides, extracted from *Stevia rebaudiana* (Asteraceae), have gained considerable attention as natural sweetening agents.[2,3] Rebaudioside A (Reb A) has attracted particular interest due to its superior organoleptic properties. Phytochemical analysis of wild *S. rebaudiana* leaves reveals a distribution of steviol glycosides comprising stevioside (9.1%), rebaudioside A (3.8%), rebaudioside C (0.6%), and glucosides (0.3%).[4] Among these glycosides, Reb A demonstrates enhanced sweetness intensity, improved stability, and reduced bitterness in comparison with stevioside.[5,6] This improvement in properties is attributed to its structural characteristics, specifically the substitution of a sophorosyl moiety with a glucosyl (1→3)-sophorosyl residue.[7]

The United States Food and Drug Administration (FDA) has granted steviol glycosides "Generally Recognised as Safe" (GRAS) status, with an Acceptable Daily Intake (ADI) of 4 mg per kg body weight.[8] Consequently, the demand for Reb A has increased due to its therapeutic potential and applications in weight management.[9] This increasing utilization in food products necessitates the development of effective analytical methods for its detection and quantification. Conventional analytical techniques for Reb A detection include high-performance liquid chromatography (HPLC),[10] liquid chromatography-mass spectrometry (LC-MS)[11] and enzyme-linked immunosorbent assay (ELISA).[12] However, these methods present several limitations, including complex instrumentation requirements, extensive sample preparation, high operational costs, and lengthy analysis times.[13] These constraints highlight the need for rapid, sensitive, and cost-effective alternatives for Reb A detection, particularly for routine quality control in food processing environments. Recent advances focus on nanostructured materials to enhance electron transfer and improve detection limits. For instance, novel electrode modifications have shown excellent reproducibility and stability in biosensing applications.[14] Advanced sensing strategies integrating nanomaterials have demonstrated superior selectivity toward target analytes.[15]

[a]*Department of Chemistry, CHRIST University, Bengaluru, 560 029, India. E-mail: ksuvardhan@gmail.com*

[b]*Centre for Renewable Energy and Environmental Sustainability, CHRIST University, Bengaluru 560 029, India. E-mail: suvardhan.k@christuniversity.in*

[c]*Department of Chemistry, Vel Tech Rangarajan Dr Sagunthala R&D Institute of Science and Technology, Avadi, Chennai, 600 062, India*

Furthermore, innovative electrode designs have enabled ultra-low detection limits for biomolecules and environmental contaminants.[16] Similarly, nanomaterial-based sensors offer promising real-time monitoring applications.[17]

Metal–organic frameworks (MOFs), a class of porous crystalline materials composed of metal ions/clusters coordinated to organic ligands, have recently attracted significant attention in biosensing applications due to their high surface area, tunable porosity, and versatile functionalization options.[18] Similarly, metal oxide nanoparticles[19] have demonstrated excellent electrocatalytic properties and electron transfer capabilities in electrochemical sensing platforms.[20,21] The integration of these nanomaterials with specific enzymes creates synergistic systems with enhanced sensitivity and selectivity.[22] In this study, we present a next-generation electrochemical biosensor for Reb A detection based on a nanocomposite of Co-MOF nanosheets, CuO NPs and Nafion in conjunction with glucose oxidase (GOx) enzyme. The Co-MOF provides a high surface area and porous structure for efficient enzyme immobilization, while CuO NPs enhance electron transfer and catalytic activity. The integration with GOx ensures selective biorecognition, making the nanocomposite highly sensitive and reliable for Reb A detection. The CuO NPs were synthesized *via* a green route using guava leaf extract, aligning with sustainable chemistry principles.[23] Meanwhile, Co-MOF nanosheets were prepared through solvothermal synthesis using cobalt chloride and terephthalic acid in *N*,*N*′-dimethylformamide (DMF).[24] This nanocomposite was deposited on a graphite electrode, followed by the incorporation of GOx.

The synergistic interaction between the CuO–Co-MOF nanosheets and GOx creates a highly sensitive platform for Reb A detection. The biosensor demonstrates several advantages over existing methods, including enhanced sensitivity, stability, and applicability for real-time analysis in complex food matrices. This is the first electrochemical biosensor utilising Co-MOF nanosheets/CuO NPs integrated with glucose oxidase (GOx) for Reb A quantification. Also, it is the second biosensor platform designed for steviol glycosides, with sensor–analyte interactions validated through molecular docking.

2. Experimental

2.1 Reagents and materials

All reagents and materials employed in this study were sourced from various commercial suppliers. KH_2PO_4 (98%), K_2HPO_4 (98%), H_2SO_4 (98%), H_3PO_4 (85%), C_2H_5OH (99%), and DMF (99.8%) were purchased from Sigma-Aldrich, India. For the analytical standards, laboratory-grade rebaudioside A (98%) was obtained from Merck India, while commercial stevia samples in powder, tablet, and drop formulations were procured from a local medical store.

2.2 Instrumentation

Multiple analytical techniques were employed for thorough characterization of the synthesized nanomaterials. XRD patterns of the Co-MOF nanosheets and CuO NPs were recorded using a Rigaku-mini flex diffractometer (Cu Kα radiation, λ = 1.5406 Å). For morphological examination, we utilized Thermo Fisher's Apreo 2S scanning electron microscope alongside a Talos F200S transmission electron microscope, with high-resolution TEM being used to provide insights into the atomic configurations. To investigate surface properties, Raman spectroscopic measurements were conducted on a Renishaw instrument equipped with a 532 nm excitation laser. The chemical states at the surface were determined through XPS analysis using a PHI Versa Probe III system (aluminum Kα X-ray source). To evaluate the optical characteristics of the CuO NPs, a Shimadzu UV-1800 spectrophotometer was employed, while their interaction with *Psidium guajava* extract was analyzed using a Shimadzu A224056 FTIR spectrometer. A Malvern Panalytical dynamic light scattering instrument was employed to measure particle size distribution (DLS) and zeta potential. For electrochemical analysis, measurements were recorded on a Metrohm Auto Lab system running Nova 2.1.5 software, utilizing a three-electrode system consisting of graphite as the working electrode, a Pt counter electrode, and an Ag/AgCl reference electrode.

2.3 Synthesis of nanomaterials

2.3.1 Biogenic synthesis of CuO NPs using *Psidium guajava* leaf extract. *Psidium guajava* leaves were chopped into tiny pieces and cleaned with double-deionised distilled water. After being dried at 50 °C in an oven, the leaves were pounded into powder with a mortar and pestle and kept in a dry location. 5.0 g of the leaf powder was mixed in 100 mL of doubly deionised distilled water, and the mixture was heated for 15 min at 60–70 °C. To improve extraction efficiency, the mixture was heated, cooled, and then aggressively agitated for 20 to 30 min using a magnetic stirrer. To separate the components, the solution was centrifuged for 10 min at 5000 rpm. After filtering the supernatant using Whatman No. 1 filter paper, the filtrate was stored at 4 °C.

A 1.0 M solution of $Cu(CH_3COOH)_2 \cdot H_2O$ was made in 20 mL of distilled water at room temperature. Then, while stirring constantly at 300 rpm, 40 mL of *Psidium guajava* leaf extract was added dropwise to the copper acetate solution. A gel formed after the mixture was agitated for 24 h at 70 °C at 300 rpm. A green precipitate was produced. This gel was dried at 60 °C in a hot air oven. This precipitate was calcined for 2 h at 400 °C to produce CuO NPs as shown in Scheme 1(a).

2.3.2 Synthesis of Co-MOF nanosheets. To synthesize Co-MOF nanosheets, 0.98 g of cobalt nitrate hexahydrate ($Co_3(NO)_3 \cdot 6H_2O$) and 0.67 g of terephthalic acid were dissolved in 25 mL of DMF and stirred for 20 min to ensure complete dissolution.[25] After that, the mixture was transferred to a Teflon-lined autoclave and heated for 15 h at 120 °C. The autoclave was allowed to cool naturally to ambient temperature. To remove unreacted components, the final product was centrifuged for 3 min at 5000 rpm and then successively cleaned with DMF and ethanol. Finally, a hot air oven was used to dry the product at 50 °C as illustrated in Scheme 1(b). This procedure yielded Co-MOF nanosheets for further applications.

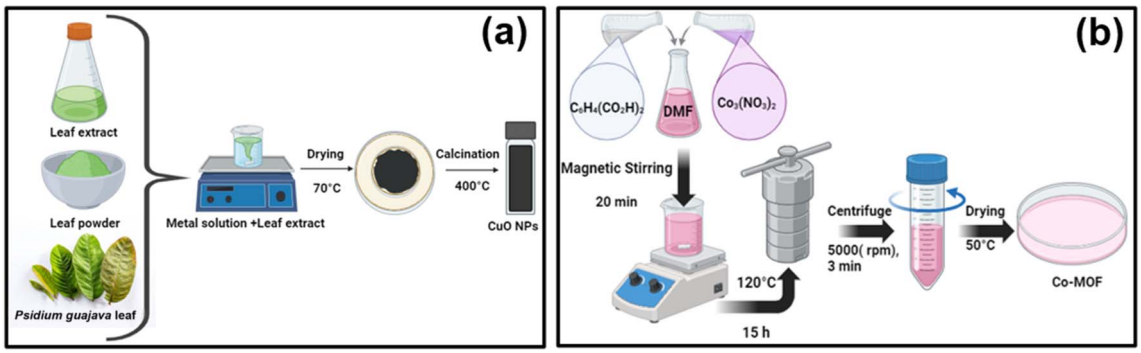

Scheme 1 (a) Biogenic synthesis of CuO NPs and (b) solvothermal synthesis of Co-MOF.

2.4 Recycling graphite (GE) rods from discharged batteries

Graphite rods were extracted from discarded household batteries, taking care to avoid leaking or corroded ones to ensure safety. The dismantling was carried out using protective equipment (goggles, gloves, and face masks) in a well-ventilated environment. The cathodic side of the battery was gently tapped with a small hammer to unseal it, after which the graphite rods were carefully pulled out using pliers without damaging their structure. The metallic cap attached to the rods was retained to facilitate their use in electrochemical studies (S.1). The recovered rods were cleaned thoroughly using sandpaper of varying grit sizes to remove residual electrolyte, followed by washing with tap water and distilled water. Subsequently, they were sonicated in isopropanol for 30 min to ensure surface purity. Finally, the rods were dried in a hot air oven at 150 °C for 48 h to eliminate moisture. The exposed surface area of the graphite rod immersed in the reaction mixture was measured to be 0.3 cm^2. This rigorous cleaning and preparation process ensures contaminant-free graphite electrodes suitable for reliable electrochemical applications (S.2).

2.5 Preparation of electrolytes and real samples

A precisely weighed Reb A was dissolved in a 10 mL volumetric flask and diluted to the appropriate level with distilled water to create a standard solution of 0.1 mM Reb A. Likewise, KH_2PO_4 and K_2HPO_4 were dissolved in 100 mL of distilled water to create a 0.1 M phosphate buffer solution (PBS). The solution was stored at 4 °C once the ideal pH of 3.0 was achieved through the quantitative addition of NaOH or H_2PO_4. To prepare a standard electrolyte, equivalent amounts of the corresponding salts were dissolved in distilled water to make a 0.1 M KCl and 5 mM potassium ferrocyanide/ferricyanide solution. Commercial Nafion (5%) was diluted using a 4 : 1 v/v mixture of ethanol and deionised water to create a 0.5% (w/v) Nafion solution. The resultant solution was sonicated for 10 min to achieve homogeneity. The necessary quantity of GOx enzyme was precisely weighed to create a 0.01 mM solution in phosphate buffer (pH 7.0) for the GOx enzyme solution. After being transferred to a volumetric container and diluted as necessary, the solution was stored at 4 °C. Stevia tablet and stevia powder formulations (0.01 g) were dissolved in 10 mL of PBS (pH 3.0), separately, sonicated for 10 min, and then centrifuged before actual sample analysis. To find the concentration of Reb A in the real samples, the supernatant was gathered and subjected to voltammetric analysis. To find the amount of Reb A in Tropicana fruit juice, 1 mL of real sample was diluted with 10 mL of phosphate buffer and sonicated well. In the same manner, 100 μL of stevia drops were dissolved in 10 mL of PBS (pH 3.0) and thoroughly sonicated to detect the Reb A present in the real sample.

2.6 Preparation and fabrication of Nafion/Co-MOF nanosheets/CuO NPs/GOx on graphite (GE)

The recovered GE from used batteries was cleaned, dried, and further coated with 2 μL of 0.5% Nafion solution and allowed to dry at ambient temperature. Separately, 0.01 g of Co-MOF nanosheets/CuO NPs were dispersed in 3 mL of DMF and ultrasonicated for 10 min to obtain a homogeneous suspension. Eventually, 1 μL of the prepared nanocomposite was drop-cast onto the GE coated with Nafion and dried at ambient temperature. The fabricated electrode was used for the electrochemical detection of Reb A.

2.7 Electrochemical measurements of Reb A with GE/Nafion/Co-MOF nanosheets/CuO NPs/GOx

An electrochemical cell was prepared with 10 mL of PBS (pH 3.0). A bare or a modified GE was positioned as the working electrode within the cell. Before analysis, multiple cyclic potential sweeps were executed until stable baseline currents were established. Subsequently, a measured aliquot was added to the electrochemical cell, and a pre-concentration step was performed by providing a set voltage to the working electrode for a predetermined period. Differential Pulse Voltammograms (DPV) were then captured and recorded using a positive-going potential scan at 0.1 V s^{-1}, utilizing either the bare or a modified GE as the working electrode.

2.8 Molecular docking study

The molecular docking computational study was done to confirm the interactions between Reb A and GOx (ligand and protein). Initially, the structure of Reb A and the crystal structure of the glucose oxidase (PDB 1GAL) were downloaded from PubChem and the PDB database, respectively. The protein was

prepared by deleting the water molecules, followed by the addition of polar hydrogens and Kollman charges using the AutoDock Tool 1.5.7 and MGL software.[26] The blind docking method was applied to prepare the grid box for the input data of 'protein.pdbqt' (GOx) and 'ligand.pdbqt' (Reb A) files. The generated 'file.gpf' and 'file.dpf' were imported for simulation using a genetic algorithm with a population size of 300 and 50 iterations.[27] The obtained results in terms of hydrogen bonding, hydrophobic interactions, and bond distance and docking score were analysed using the Biovia Discovery Studio.

3. Results and discussion

3.1 Characterization of the CuO NPs/Cu-MOF nanosheet composite

The structural and optical properties of the biogenic CuO NPs were thoroughly investigated using various analytical techniques. UV-Visible spectroscopy revealed a characteristic absorption peak at 274 nm, confirming the formation of CuO NPs through the surface plasmon resonance (SPR) phenomenon (Fig. 1(a)).[28] The optical band gap, estimated from the Tauc plot, was found to be 4.56 eV, indicating a wide band gap typical of nanoscale CuO with possible quantum confinement effects (S.3).[29] The FTIR analysis (Fig. 1(b)) confirmed the involvement of functional groups such as O–H, C=O, and C–H from the *Psidium guajava* leaf extract in the reduction and stabilization of the nanoparticles.[30] A prominent peak at 522 cm^{-1} further confirmed the presence of Cu–O bonds.[31]

The zeta potential analysis (S.4) showed a surface charge of −23.6 mV, suggesting good colloidal stability due to electrostatic repulsion. DLS analysis (S.5) revealed a *Z*-average particle size of ~374.7 nm and a polydispersity index (PDI) value of 0.386, indicating moderate size distribution and some degree of nanoparticle aggregation in suspension. The findings validate that *Psidium guajava* leaf extract was successfully used for the synthesis and stabilisation of CuO-NPs.

The morphology of CuO NPs and Co-MOF nanosheets was characterized by SEM. The SEM images of CuO NPs exhibit a spherical morphology[32] with an average diameter of ~24.1 nm, as shown in Fig. 2(a). The morphology of the Co-MOF was observed as nanosheets with protrusions on the surface, stacked over one another, indicating increased surface porosity (Fig. 2(b)). The EDS analysis of CuO NPs and Co-MOF nanosheets confirms the presence of Cu and O elements for CuO NPs, and Co, C, and O elements for Co-MOF (S.6 and S.7), confirming the successful preparation of these nanomaterials. The heterogeneous distribution of the component nanomaterials within the nanocomposite can be identified from Fig. 2(c), which shows the distinct spatial arrangement of both CuO NPs and Co-MOF nanosheets.

Distinct lattice fringes with interplanar spacings of 0.450 nm and 0.133 nm were visible in the HRTEM images of Co-MOF nanosheets (Fig. 2(d) and (e)). These fringes can be attributed to the (001) and (110) crystallographic planes of the Co-MOF and CuO NP structure. The detailed TEM analysis of the Co-MOF sheet-like structure aligns well with the SEM results. The strong integration of both nanostructures in the composite is confirmed by HRTEM analysis, which shows CuO NPs dispersed randomly on the Co-MOF nanosheets (Fig. 2(f)). The crystalline nature of the nanocomposite is verified by the selected area electron diffraction (SAED) pattern.

The characteristic peaks for CuO NPs were observed at 2θ values of 32.4°, 35.5°, 38.6°, 48.8°, 53.3°, 58.2°, 61.5°, 66.3°, 67.8°, 72.3°, and 75.2°. These diffraction peaks correspond to the (110), (110), (111), (202), (020), (202), (113), (311), (113), (311), and (222) crystallographic planes, respectively. The peak positions and patterns match the standard JCPDS card no. 89-2529, confirming a face-centered cubic structure with a monoclinic phase.[33] The well-defined diffraction peaks show that the synthesized CuO NPs possess a crystalline structure. The (001), (101), (200), (321), (001), and (325) crystallographic planes at 2θ values of 9.65°, 15°, 18.7°, 20.1°, 29.5°, and 33.7° correspond to the Co-MOF nanosheets. These characteristic peaks match perfectly with the previously reported diffraction patterns of cobalt terephthalate hydroxide [$Co_2(OH)_2C_8H_4O_4$], validating the successful synthesis of the Co-MOF nanosheets.[34] The coexistence of diffraction peaks from both components confirms the formation of a composite material without structural degradation of the individual phases as depicted in Fig. 3(a).

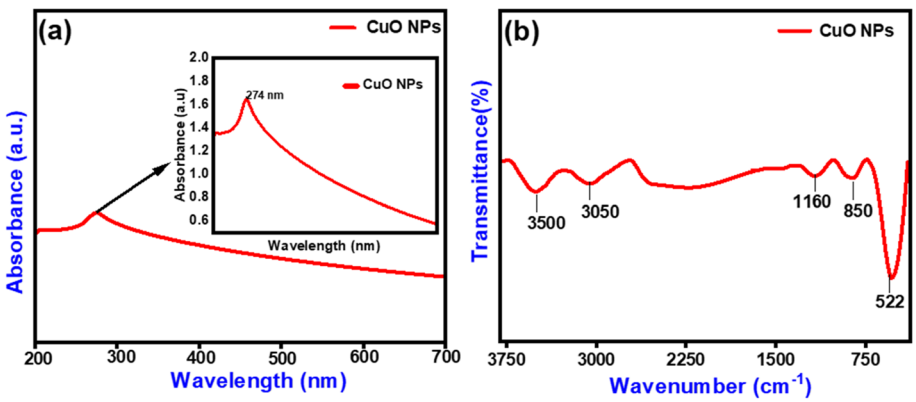

Fig. 1 Characterization of CuO NPs synthesized using *Psidium guajava* leaf extract: (a) UV-vis spectra showing an absorption peak at 274 nm; and (b) FTIR spectra confirming functional groups and Cu–O bonds at 522 cm^{-1}.

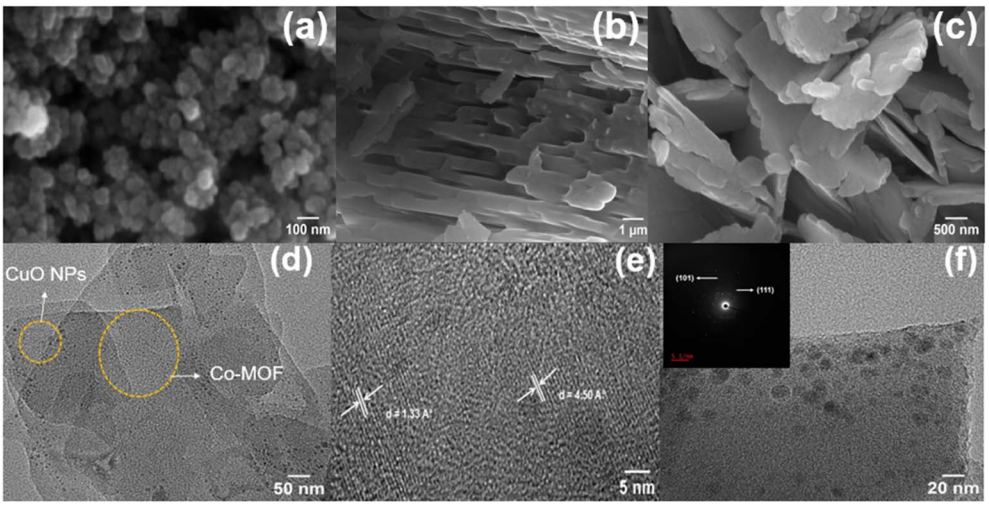

Fig. 2 (a) SEM images of biosynthesized CuO NPs, (b) Co-MOF nanosheets, and (c) CuO/Co-MOF nanosheet composite; (d and f) TEM images of CuO NPs/Co-MOF nanosheets; (e) HRTEM image displaying lattice fringes; inset shows SAED pattern.

The Raman spectroscopy analysis reveals distinct vibrational signatures of each component in the CuO NPs/Co-MOF nanosheet composite system (Fig. 3(b)). The Co-MOF nanosheets exhibit characteristic bands at 862, 1143, 1432, and 1618 cm^{-1}, corresponding to vibrations within the benzene-1,4-dicarboxylate linkers, specifically the C–H bending mode, C–O stretching mode, and aromatic C=C stretching mode. Low-frequency peaks below 401 cm^{-1} indicate Co–O vibrations at the metal nodes.[35] The CuO NPs display three diagnostic modes: a sharp Ag mode at 287 cm^{-1} (in-phase oxygen motion perpendicular to Cu–O–Cu chains), a less intense Bg(1) mode at 345 cm^{-1} (oxygen atom vibrations), and a broad Bg(2) mode at 602 cm^{-1} (Cu–O stretching along the [101] plane direction), with peak broadening indicative of nano-dimensional phonon confinement effects.[36] The composite spectrum showcases all characteristic bands from both materials, confirming successful formation of a heterogeneous system where both components maintain their structural integrity while creating interfacial junctions.

The XPS analysis verified the presence of Cu, O, Co, and C (used as a reference) elements in the synthesized nanocomposite (CuO NPs/Co-MOF nanosheets). Fig. 4(a) shows the survey XPS spectra of the CuO NPs/Co-MOF nanosheet composite, which confirms the presence of Cu, O, Co, and C elements. The peaks observed at 933.4 eV and 953.4 eV represent Cu $2p_{3/2}$ and Cu $2p_{1/2}$, respectively, with a spin energy separation of 20 eV. The satellite peaks at 937.7 eV and 959.7 eV confirm the presence of Cu^{2+} in the synthesized composite. The broader satellite peak at 937.7 eV results from charge transfer shake-up satellite transitions typical of Cu^{2+} ions, occurring when photoionization induces electron transitions between ligand orbitals and a partially filled 3d shell of copper. This confirms the presence of Cu^{2+} in the composite (Fig. 4(b)). The O 1s XPS spectrum revealed two distinct oxygen environments in the composite material. The signal at 531.4 eV confirms oxygen species participating in Cu–O bonding, characteristic of CuO NPs.[37] Meanwhile, the peak detected at 532.2 eV, as shown in Fig. 4(c), can be assigned to the carbonyl oxygen (=O) present in the carboxylic acid functional groups that constitute the organic linkers of the Co-MOF nanosheets.

This spectral evidence delineates the dual oxygen environments within the CuO NPs/Co-MOF nanosheet composite. The

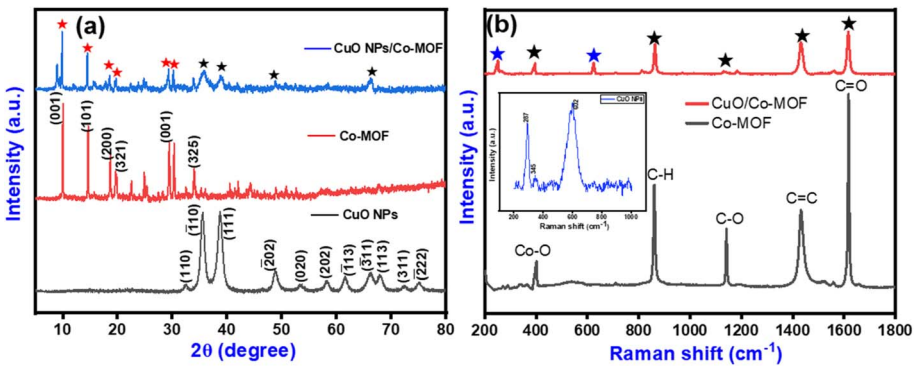

Fig. 3 (a) XRD analysis of CuO NPs, Co-MOF nanosheets, and CuO/Co-MOF composite. (b) Raman analysis of Co-MOF nanosheets and CuO/Co-MOF nanosheets.

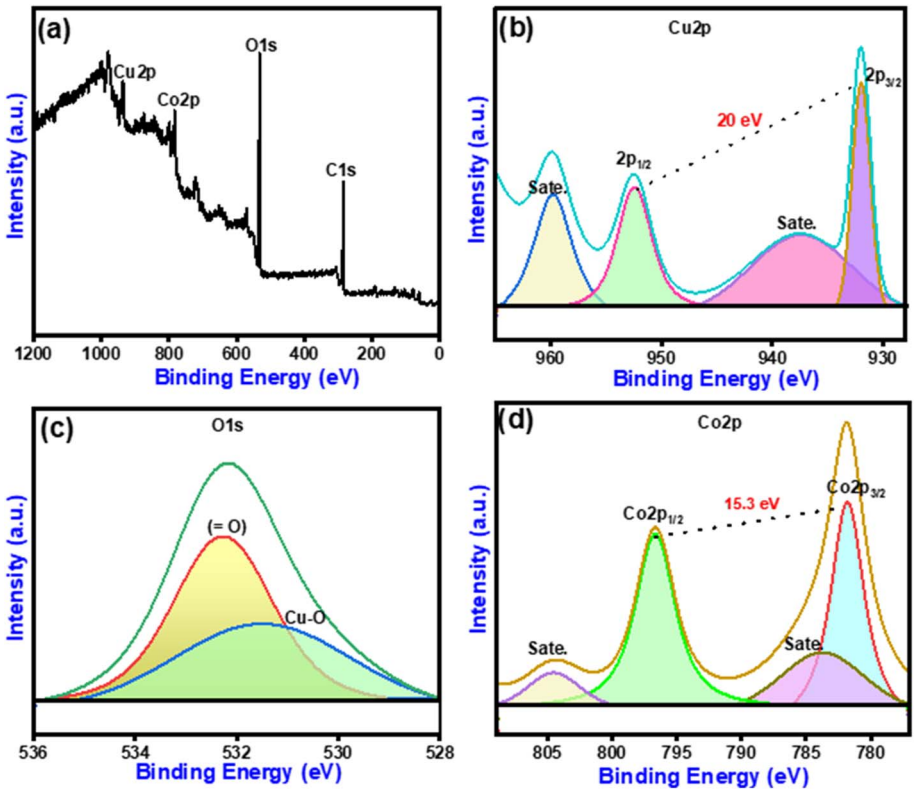

Fig. 4 XPS spectra of the CuO NPs/Co-MOF nanosheet composite showing (a) the survey scan with elemental peaks, (b) Cu 2p, (c) O 1s, and (d) Co 2p.

Co 2p XPS spectrum analysis (Fig. 4(d)) exhibits two primary photoelectron peaks positioned at 781.5 eV and 796.8 eV, displaying a characteristic spin–orbit splitting energy of 15.3 eV. These signals correspond to the Co $2p_{3/2}$ and Co $2p_{1/2}$ core-level transitions, respectively. Additionally, satellite features are observed at higher binding energies of 783.7 eV and 803.4 eV.[38] The binding energy positions, spin–orbit coupling parameters, and the presence of these distinctive satellite structures are consistent with the electronic configuration of Co^{2+} ions in an octahedral coordination environment within the metal–organic framework structure.

3.2 Electrochemical characterization of GE/Nafion/Co-MOF nanosheets/CuO NPs/GOx

Electrochemical impedance spectroscopy (EIS) was performed to evaluate the charge transfer characteristics of the electrode system.[39] The investigation utilized a 5.0 mM $K_3[Fe(CN)_6]^{3-/4-}$ solution with fabricated electrode configurations comprising GE/Nafion/CuO NPs/Co-MOF nanosheets/GOx. The Nyquist plot illustrated distinctive impedance profiles for each electrode modification: GE, GE/Nafion, GE/Nafion/Co-MOF nanosheets, GE/Nafion/Co-MOF nanosheets/CuO NPs and GE/Nafion/Co-MOF nanosheets/CuO NPs/GOx as shown in Fig. 5(a). The EIS data were analyzed using an equivalent circuit model incorporating double-layer capacitance (C_{dl}), charge transfer resistance (R_{ct}), solution resistance (R_s), and Warburg impedance (W) elements.[40] Quantitative analysis revealed charge transfer resistance (R_{ct}) values of 70.95 Ω, 57.55 Ω, 45.70 Ω, 25.66 Ω, and 18.57 Ω for GE, GE/Nafion, GE/Nafion/Co-MOF nanosheets, GE/Nafion/Co-MOF nanosheets/CuO NPs, and GE/Nafion/Co-MOF nanosheet/CuO NPs/GOx, respectively. The significantly reduced R_{ct} value observed for the GE/Nafion/CuO NPs/Co-MOF nanosheets/GOx modified electrode indicates higher electron transfer kinetics and superior conductivity compared to the other electrode configurations.

The microscopic areas of the developed sensor were investigated using the same $[Fe(CN)6]^{4-/3-}$ and decimolar KCl electrolyte.[41] The analysis was performed using the cyclic voltammetry technique at a scan rate of 0.05 V s^{-1}, as shown in Fig. 5(b). The effective surface area of the electrodes was calculated by graphical examination of the correlation between anodic peak currents and the square root of scan rates. The slopes obtained from these plots were then utilized in conjunction with the Randles–Sevcik equation (eqn (1)).[42]

$$I_{pa} = 2.69 \times 10^5 A C_0 n^{3/2} D_R{}^{1/2} \nu^{1/2} \quad (1)$$

A denotes the electroactive surface area (cm^2), D_0 is the diffusion coefficient (cm^2 s^{-1}), n is the number of electrons participating in the electrochemical redox reaction, ν is the scan rate in V s^{-1}, and C is the concentration of $K_3[Fe(CN)_6]$ in the bulk solution in mol cm^{-3}. The surface area calculated for bare GE, GE/Nafion, GE/Nafion/Co-MOF nanosheets, GE/Nafion/Co-MOF nanosheets/CuO NPs, and GE/Nafion/Co-MOF nanosheets/CuO NPs/GOx was found to be 0.0052, 0.0074, 0.013, 0.118,

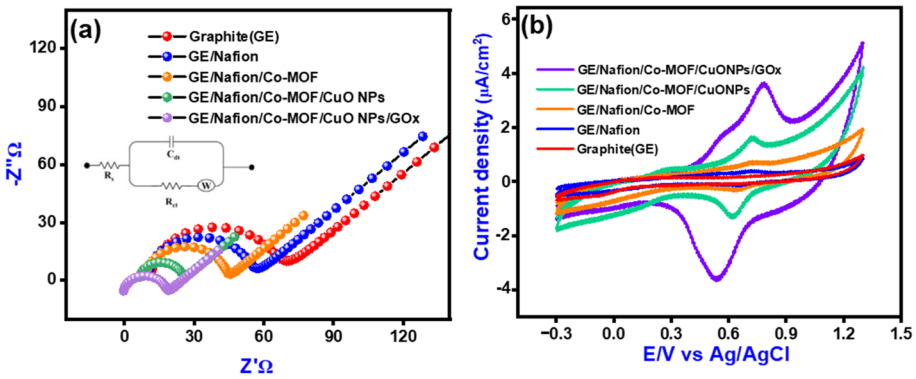

Fig. 5 (a) Electrochemical Impedance Spectroscopy (EIS) profiles for bare GE, GE/Nafion, GE/Nafion/Co-MOF nanosheets, GE/Nafion/Co-MOF nanosheets/CuO NPs and GE/Nafion/Co-MOF nanosheets/CuO NPs/GOx; and (b) cyclic voltammetry (CV) responses in 5.0 mM $[Fe(CN)_6]^{3-}/^{4-}$ with 0.1 M KCl using the same set of electrodes.

and 0.209 cm^2, respectively. The surface area calculated for the bare GE is much lower than that of the modified GE/Nafion/Co-MOF nanosheet/CuO NPs/GOx electrode.

3.3 Method optimization

The influence of pH on the electrochemical behaviour of the Nafion/Co-MOF nanosheets/CuO NPs/GOx was systematically investigated using phosphate buffer solutions (PBS) ranging from pH 2.0 to 7.0 as shown in Fig. 6(a). The electrochemical response exhibited a strong pH-dependent pattern, with the maximum potential and oxidation current observed at pH 3.0, suggesting optimal conditions for Reb A detection. The observed decline in potential from pH 2.0 to 7.0 (slope = −0.026, intercept = 0.192) (S.8) indicates a proton-coupled electron transfer mechanism.[43] This behaviour is due to the synergistic impact of the electrode components: the Co-MOF nanosheets and CuO NPs demonstrate enhanced stability and electrochemical activity under mildly acidic conditions, while the Nafion membrane's proton conductivity is optimized. The slightly decreased performance at pH 2.0 compared to pH 3.0

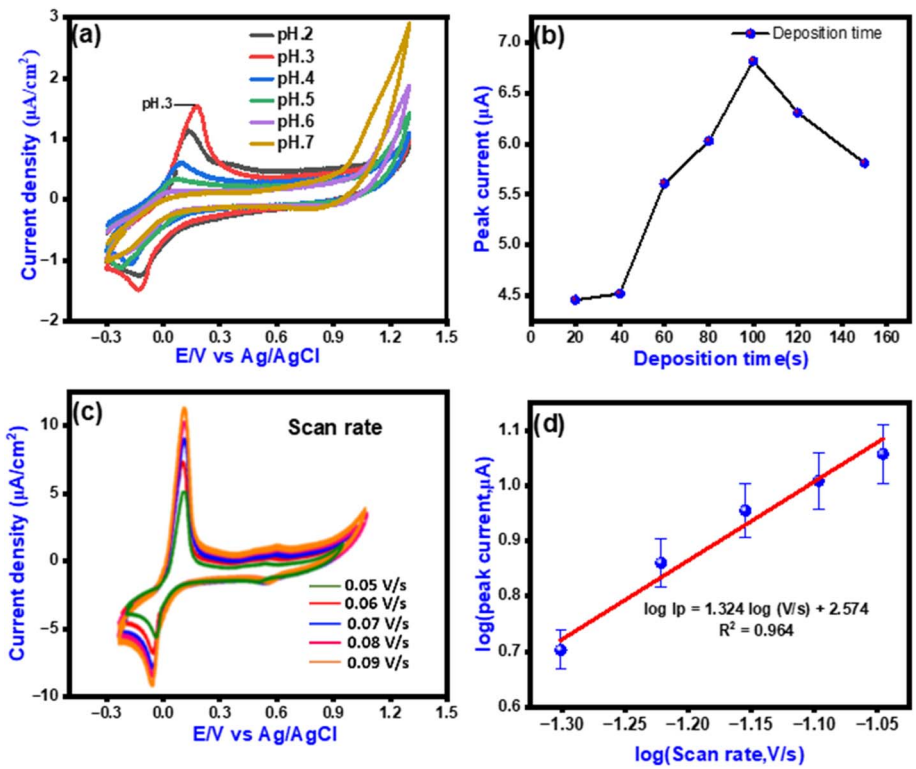

Fig. 6 (a) Cyclic voltammograms at different pH values (2.0–7.0) using the GE/Nafion/Co-MOF nanosheets/CuO NPs modified electrode. (b) Peak current response as a function of deposition time (20–160 s). (c) Cyclic voltammograms (CVs) at varying scan rates from 0.05 to 0.09 V s^{-1}. (d) Log–log plot of peak current *vs.* scan rate.

suggests that extremely acidic conditions may affect the stability of the Co-MOF nanosheets and overall electrode surface chemistry.[44] The strong linear correlation ($R^2 = 0.93$) between pH and potential (S.3) confirms the reliability and reproducibility of the electrochemical sensing system, validating the electrode's effectiveness for Reb A detection under controlled pH conditions.

The electrochemical performance of the GE/Nafion/Co-MOF nanosheets/CuO NPs/GOx modified electrode was optimized by evaluating the effects of deposition time and scan rate. As shown in Fig. 6(b), the peak current increased with deposition time, reaching a maximum at 100 s; beyond this point, the current declined, likely due to surface saturation or limited diffusion, indicating that 100 s is the optimal deposition time. The influence of scan rate (0.05–0.09 V s^{-1}) was studied using cyclic voltammetry (Fig. 6(c)), where an increase in scan rate led to a proportional rise in peak current, suggesting a diffusion-influenced or mixed-controlled process. A log–log plot of peak current *versus* scan rate was created to investigate further the electrochemical mechanism (Fig. 6(d)), yielding a linear relationship with a slope of 1.324 and $R^2 = 0.964$. The slope value, greater than unity, indicates that the electrochemical process is predominantly adsorption-controlled, reflecting strong analyte interaction with the electrode surface facilitated by the Co-MOF nanosheets/CuO NPs/GOx, thus enhancing the electrochemical response.

3.4 Redox mechanism of Reb A at GE/Nafion/Co-MOF nanosheets/CuO NPs/GOx

The electrochemical detection of Reb A at the GE/Nafion/Co-MOF nanosheets/CuO NPs/GOx modified electrode can be due to the synergistic interaction between the electrode components as shown in Fig. 7.

The observed sharp oxidation peak at 0.16 V corresponds to the electrochemical oxidation of carbonyl groups of the Reb A structure[45] as depicted in Scheme 2. This oxidation process is mediated by the Cu(II)/Cu(III) redox couple within the CuO NPs,

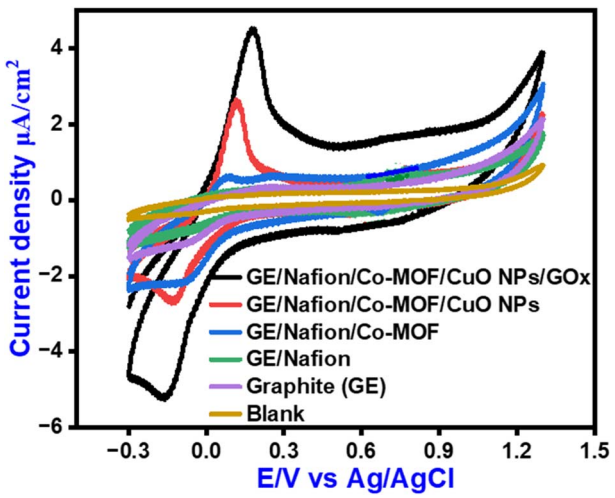

Fig. 7 Cyclic voltammogram response of bare and modified graphite electrodes for Reb A.

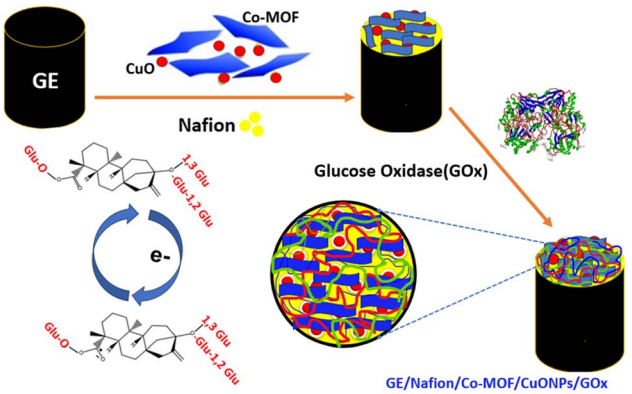

Scheme 2 A possible pathway for the electrochemical oxidation of Reb A.

which serves as an electron transport bridge between the Reb A and the modified electrode surface. Concurrently, the Co-MOF nanosheets enhance the catalytic efficiency through their well-defined porous structure and abundant active sites. The smaller reduction peak at −0.17 V likely represents the reduction of previously oxidized species. Furthermore, GOx contributes to the sensing mechanism by recognizing the glycosidic structures in Reb A and potentially generating hydrogen peroxide as a reaction byproduct,[46] amplifying the electrochemical signal. The Nafion polymer effectively improves selectivity by allowing preferential permeation of the target analyte while excluding potential interfering substances.[47]

3.5 Quantitative detection of Reb A

Differential Pulse Voltammetry (DPV) was employed for the qualitative determination of Reb A using 0.1 mM analyte. The standard addition method was applied by successive introduction of 200 µL aliquots into 10 mL of phosphate buffer (0.1 M). DPV, which measures the current response to potential pulses superimposed on a linear sweep, revealed distinct shifts in the oxidation peak potentials with increasing Reb A concentration at the GE/Nafion/Co-MOF/CuO NPs/GOx sensor surface. These progressive shifts indicate an enhanced potential requirement for the electro-oxidation process, thereby confirming the interaction and electroactive nature of Reb A. The observed peak current (I_{pa}) responses further established a concentration-dependent trend, with a well-defined linear dynamic range (2.0–14.0 µM), as shown in Fig. 8(a) and (b), thus validating the sensor's capability for reliable qualitative and semi-quantitative assessment of Reb A. The calibration plot followed the linear regression equation:

$$I_{pa}\ (\mu A) = 0.113C_i + 0.618I,\ (R^2 = 0.993). \quad (2)$$

The method exhibited excellent analytical sensitivity, resulting in a limit of detection (LOD) of 0.23 µM and a limit of quantification (LOQ) of 0.78 µM.

The LOD and LOQ were calculated using formulae $3\sigma/m$ and $10\sigma/m$, where 'm' represents the slope of the calibration curve

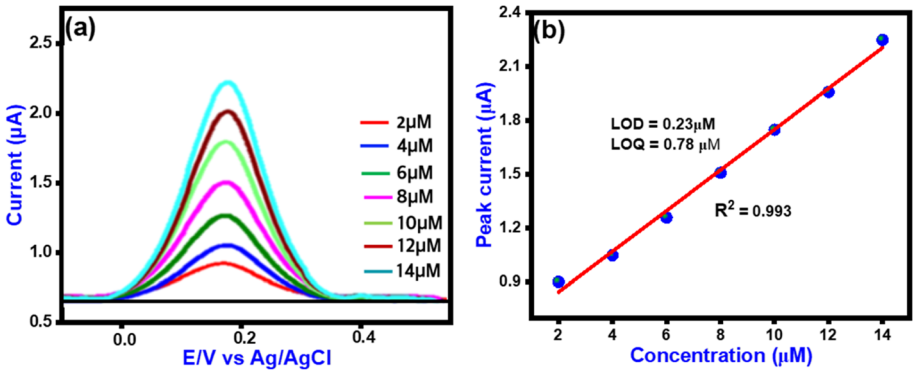

Fig. 8 (a) Differential pulse voltammetry of GE/Nafion/Co-MOF nanosheets/CuO NPs at a linear dynamic range of 2–14 μM using 0.1 M PBS (pH 6.0). (b) I_{pa} (μA) *vs.* concentration (μM) calibration curve.

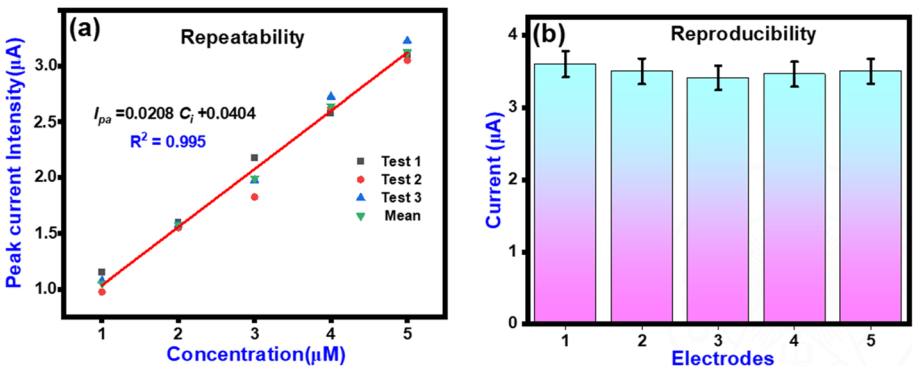

Fig. 9 Validation of (a) the repeatability and stability, and (b) the reproducibility of the GE/Nafion/Co-MOF nanosheets/CuO NPs/GOx.

and 'σ' represents the standard deviation of the background current obtained from triplicate blank measurements. This calculation is based on a signal-to-noise ratio of 3, as shown in Fig. 8(b). The sensor demonstrates high sensitivity and a low detection limit due to the synergistic effects of the electrode surface modifications. The results demonstrate that the developed sensor exhibits high sensitivity for determining Reb A in real samples, making it suitable for practical analytical applications.

3.6 Validation of GE/Nafion/Co-MOF nanosheets/CuO NPs/GOx

The fabricated electrode was evaluated for repeatability and stability by performing three consecutive measurements with the same sensor at Reb A concentrations ranging from 1 to 5 μM (within the first linear range). As shown in Fig. 9(a), the calibration curves from three independent tests (test 1, test 2, and test 3) exhibited highly consistent responses. The mean calibration curve (red line) indicates a linear relationship represented by the equation $I_{pa} = 0.0208C_i + 0.0404$, where the sensitivity is 0.0208 μA μM^{-1} and the correlation coefficient (R^2) is 0.9996. The overlap of the three individual test curves with the mean curve demonstrates excellent repeatability and stability of the sensor, with minimal variation between consecutive measurements. Reproducibility was evaluated using differential pulse voltammetry (DPV) with five independently fabricated GE/Nafion/Co-MOF nanosheets/CuO NPs/GOx modified electrodes prepared under identical conditions. Each electrode was tested for Reb A detection at the same concentration. As shown in Fig. 9(b), all five electrodes exhibited consistent peak current responses, with values ranging approximately from 3.6 to 3.7 μA. The relative standard deviation (RSD) calculated from these measurements was 3.9%, which is well below the acceptable threshold of 5% for electrochemical sensors. This low RSD value demonstrates excellent reproducibility of the fabrication process and confirms the reliability of the sensor for quantitative analysis.

The analytical performance of the proposed method was evaluated through intra-day precision and accuracy studies using standard Reb A solutions at three concentration levels (0.2, 0.4, and 0.6 mM) with triplicate analysis ($n = 3$). Method validation parameters demonstrated excellent analytical performance, with relative bias values ranging from −0.03 to −0.018, indicating minimal systematic error. The precision, expressed as relative standard deviation (RSD), ranged from 0.91% to 1.36%, demonstrating acceptable reproducibility well within the typically accepted criterion of <2% for analytical methods. Recovery studies yielded values between 97.00% and 98.17%, confirming the method's accuracy and absence of significant matrix interference effects as given in Table 1.

Table 1 Analytical parameters (accuracy, precision, and recovery ($n = 3$)) obtained for Reb A

Added (mM)	Found (mM)	Bias[a]	Recovery[b] (%)	RSD[c] (%)
0.2	0.194	−0.03	97	1.36
0.4	0.391	−0.022	97.75	1.24
0.6	0.589	−0.018	98.17	0.91

[a] Bias = (found − added/added). [b] Average calculated from three independent readings. [c] Relative standard deviation for three independent determinations.

3.7 Application to real samples

Real sample analysis of Reb A was conducted using four commercially available products: stevia (in tablet, powder, and drop forms) and Tropicana (in soft drink form). A control sample with 0.2 mM Reb A yielded a measured concentration of 0.194 mM, which served as the reference for calculating recovery percentages and relative standard deviations (RSD%). Each sample was spiked with two different concentrations to evaluate method accuracy.

The recovery values ranged from 90.0% to 93.3%, indicating high accuracy and minimal matrix interference across diverse sample types. The RSD values, ranging from 1.12% to 1.34%, confirm the excellent repeatability and precision of the developed electrochemical method as mentioned in Table 2. The consistent recovery rates and low RSD% values validate the method's reliability for quantifying Reb A in various commercial formulations, including liquids and solids. This confirms the method's applicability for routine quality control and authenticity checks of stevia-based sweetener products in real food matrices.

3.8 Interference study

To evaluate the selectivity of the developed electrochemical sensor towards Reb A, an interference study was performed by comparing the relative current response of Reb A with various potentially interfering agents commonly present in commercial sweetener formulations, as illustrated in Fig. 10.

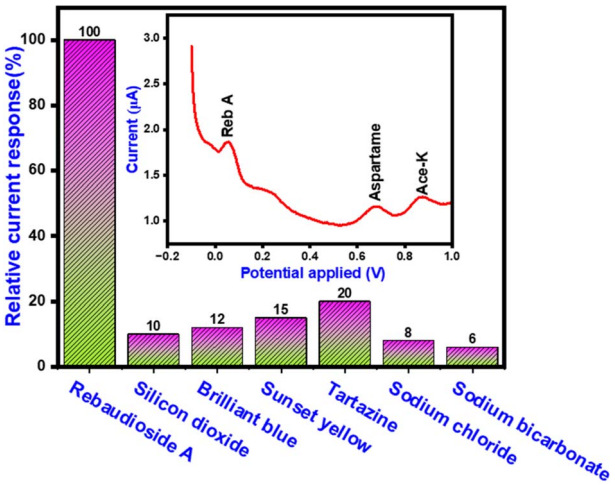

Fig. 10 Relative current response of Reb A and potential interferents, demonstrating high selectivity of the sensor. Inset: DPV curve showing distinct peaks for Reb A, aspartame, and acesulfame-K.

Reb A exhibited a pronounced and distinct electrochemical response, with a normalized relative current response of 100%, confirming its strong interaction with the sensing platform. In contrast, common excipients and additives such as silicon dioxide, brilliant blue, sunset yellow, tartrazine, sodium chloride, and sodium bicarbonate exhibited significantly lower current responses, ranging from 6% to 20%. Among these, tartrazine showed the highest interference (20%), followed by sunset yellow (15%), brilliant blue (12%), silicon dioxide (10%), sodium chloride (8%), and sodium bicarbonate (6%).

These results indicate minimal interference from these substances, affirming the high selectivity of the sensor towards Reb A. The inset of Fig. 10 presents a differential pulse voltammetry (DPV) curve, where clear and well-resolved peaks corresponding to Reb A, aspartame,[48] and acesulfame potassium (Ace-K)[49] are observed at different potentials. Glucose and fructose were also added along with the analyte, but no oxidation peak was observed within this potential window. The distinct oxidation potential of Reb A, compared to other

Table 2 Detection of Reb A in real samples

Sample	Added (mM)	Found (mM)	Recovery[e] (%)	RSD[e,f] (%)
Stevia (tablet)[a]	—	0.194	—	—
	0.15	0.320	93.3	1.18
	0.3	0.461	93.0	1.21
Stevia (powder)[b]	—	0.194	—	—
	0.15	0.331	91.4	1.19
	0.3	0.470	92.0	1.16
Stevia (drops)[c]	—	0.194	—	—
	0.3	0.470	92.1	1.34
	0.6	0.75	93.3	1.30
Tropicana[d] (soft drink)	—	0.194	—	—
	0.1	0.284	90.0	1.12
	0.2	0.076	92.4	1.14

[a] Higher Health Sciences, Mumbai, LLP, India. [b] Nutritive Advance Health Care, Pvt. India. [c] VIStevia Agro, India. [d] PepsiCo, India. [e] Average calculated from three independent readings. [f] Relative standard deviation for three individual determinations.

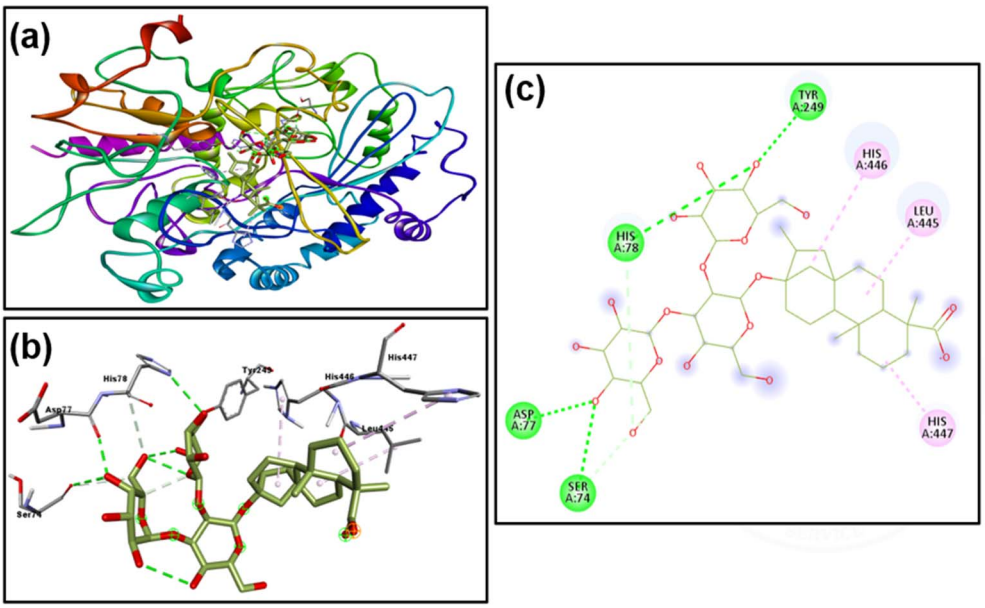

Fig. 11 Molecular docking of Reb A with GOx showing (a) overall binding conformation, (b) 3D interaction with active site residues, and (c) 2D interaction map highlighting key hydrogen bonds and hydrophobic contacts.

sweeteners, further supports the specificity of the sensor system. The absence of significant peak overlap confirms that the sensor is capable of distinguishing Reb A from structurally and functionally similar compounds.

From the literature survey (ST.1), it was observed that this is the second reported electrochemical biosensor platform for the detection of Reb A. The present work utilizes a waste-derived graphite electrode, modified with promising nanomaterials such as Co-MOF and CuO NPs, and demonstrates excellent results with high reproducibility.

4. Molecular docking studies

To analyse the molecular interactions between Reb A and glucose oxidase (GOx), a molecular docking study was conducted.[50] The docking was performed using AutoDock 1.5.7 and the MGL tool, and the most favourable binding pose (cluster rank 1) was identified with a binding energy of −7.26 kcal mol^{-1}, indicating a strong and energetically favourable interaction. Fig. 11(a) depicts the overall 3D conformation of the GOx enzyme in complex with Reb A. The enzyme is represented as a ribbon model with distinct secondary structures coloured differently to highlight its topology. The bound ligand (Reb A) is shown in the active site, interacting with key residues. Fig. 11(b) offers a closer 3D view of the docking site, illustrating specific amino acid residues of GOx involved in interactions with Reb A. Key hydrogen bonding and hydrophobic contacts are visible. Notable interacting residues include Ser74, Asp77, His78, Tyr249, Leu445, His446, and His447. These residues are strategically positioned around the ligand, facilitating stable binding through hydrogen bonds (green dashed lines), van der Waals forces, and π-stacking interactions (purple lines).

Fig. 11(c) provides a 2D interaction map of the Reb A–GOx complex, summarizing the binding interactions. Hydrogen bonds are predominantly formed with Ser74, Asp77, His78, and Tyr249. Hydrophobic interactions are primarily observed with Leu445 and His446, while His447 also participates in stabilizing the complex. This visualization confirms the orientation and anchoring of Reb A within the active pocket of GOx. The docking analysis suggests that the Reb A molecule fits well into the binding pocket of GOx and forms a network of favourable interactions that may support its potential role in enzyme recognition or inhibition.

Importantly, the experimental results are well-aligned with the theoretical findings. In the electrochemical study, using GOx in conjunction with Nafion, Co-MOF nanosheets, and CuO NPs led to a significant signal amplification, confirming the enzyme's successful molecular recognition of Reb A. The intensified oxidation peak was observed at 0.16 V, suggesting that the presence of GOx enhances the electron transfer kinetics and contributes to the specificity of the response. The molecular docking analysis supports and confirms this observation by demonstrating Reb A's favourable orientation and tight binding within the GOx active site. Together, the experimental and computational studies reinforce the finding that GOx exhibits strong affinity toward Reb A, enabling its vital use in biosensing platforms or enzymatic degradation applications targeting non-nutritive sweeteners like Reb A.

5. Conclusion

A responsive and reliable electrochemical biosensor was successfully fabricated using GE/Nafion/Co-MOF nanosheets/CuO NPs/GOx for the detection of Reb A. The synergistic integration of Co-MOF nanosheets/CuO NPs/GOx on the surface of

GE modified with Nafion significantly enhanced the electron transfer and sensing efficiency. The biosensor demonstrated a low detection limit, a wider linear range, and excellent selectivity even in the presence of potential interfering agents. Real sample analysis confirmed its practical applicability with satisfactory recovery rates. Molecular docking studies revealed favourable interactions between Reb A and GOx, validating the biosensor's molecular recognition mechanism. Overall, this biosensing platform offers a cost-effective and reliable strategy for the monitoring of rebaudioside A in food and pharmaceutical formulations.

Author contributions

Manju Manuel: original draft, visualization, validation, methodology, investigation. Venkatramana Losetty: visualization, validation, software, methodology. Suvardhan Kanchi: editing, supervision, project administration, funding acquisition, conceptualization.

Conflicts of interest

There are no conflicts to declare.

Data availability

The data supporting this article have been included as part of the SI. See DOI: https://doi.org/10.1039/d5na00591d.

Acknowledgements

The authors gratefully acknowledge the funding provided by the Centre for Research, CHRIST University in the form of seed funding with ref. no. CU-ORS-SM-24/70.

References

1 Y. Patel, O. M. Elfadil, S. Patel, O. M. Ghanem, R. T. Hurt and M. S. Mundi, Rediscovering Sweetness: The Evolution and Impact of Non-Nutritive and Natural Sweeteners, *Curr. Nutr. Rep.*, 2025, **14**(1), 54, DOI: 10.1007/s13668-025-00646-z.

2 A. M. Orellana-Paucar, Steviol Glycosides from Stevia rebaudiana: An Updated Overview of Their Sweetening Activity, Pharmacological Properties, and Safety Aspects, *Molecules*, 2023, **28**(3), 1258, DOI: 10.3390/molecules28031258.

3 M. Libik-Konieczny, E. Capecka, M. Tuleja and R. Konieczny, Synthesis and production of steviol glycosides: recent research trends and perspectives, *Appl. Microbiol. Biotechnol.*, 2021, **105**(10), 3883–3900, DOI: 10.1007/s00253-021-11306-x.

4 U. Wölwer-Rieck, Analysis of Steviol Glycosides, in *Steviol Glycosides: Cultivation, Processing, Analysis and Applications in Food*, ed. U. Wölwer-Rieck, The Royal Society of Chemistry, 2018, DOI: 10.1039/9781788010559-00084.

5 X. Tian, F. Zhong and Y. Xia, Dynamic characteristics of sweetness and bitterness and their correlation with chemical structures for six steviol glycosides, *Food Res. Int.*, 2022, **151**, 110848, DOI: 10.1016/j.foodres.2021.110848.

6 R. Tao and S. Cho, Consumer-Based Sensory Characterization of Steviol Glycosides (Rebaudioside A, D, and M), *Foods*, 2020, **9**(8), 1026, DOI: 10.3390/foods9081026.

7 A. Muñoz-Labrador, *et al.*, Transglycosylation of Steviol Glycosides and Rebaudioside A: Synthesis Optimization, Structural Analysis and Sensory Profiles, *Foods*, 2020, **9**(12), 1753, DOI: 10.3390/foods9121753.

8 J. D. Perrier, J. J. Mihalov and S. J. Carlson, FDA regulatory approach to steviol glycosides, *Food Chem. Toxicol.*, 2018, **122**, 132–142, DOI: 10.1016/j.fct.2018.09.062.

9 J. Li, P. Thaker, D. Jiang, Q. Huang and C.-T. Ho, Herb Stevia rebaudiana's functionalities, safety and applications: a review, *Nutr. Food Sci.*, 2023, **53**(8), 1373–1405, DOI: 10.1108/NFS-03-2023-0051.

10 S. Fayaz, R. Sharma, Y. S. Rajput, B. Mann and K. Lata, Estimation of steviol glycosides in food matrices by high performance liquid chromatography, *J. Food Sci. Technol.*, 2018, **55**(8), 3325–3334, DOI: 10.1007/s13197-018-3270-3.

11 S. Y. Lee and K. Shaari, LC–MS metabolomics analysis of Bertoni leaves cultivated in Malaysia in relation to different developmental stages, *Phytochem. Anal.*, 2022, **33**(2), 249–261, DOI: 10.1002/pca.3084.

12 F. Noya-Leal, *et al.*, Rebaudioside A from Stevia rebaudiana stimulates GLP-1 release by enteroendocrine cells via bitter taste signalling pathways, *Food Funct.*, 2023, **14**(15), 6914–6928.

13 Y. Phungsiangdee, P. Chaothong, W. Karnpanit and P. Tanaviyutpakdee, Validation of UHPLC-ESI-MS/MS Method for Determining Steviol Glycoside and Its Derivatives in Foods and Beverages, *Foods*, 2023, **12**(21), 3941, DOI: 10.3390/foods12213941.

14 Y. Xia, *et al.*, Mesoporous SiO2 Sphere-Based Electrochemical Impedance Immunosensor for Ultrasensitive Detection of Bovine Interferon-γ, *J. Anal. Test.*, 2023, **7**(3), 295–303, DOI: 10.1007/s41664-023-00255-1.

15 Y. Xia, *et al.*, In Situ Electrospinning MOF-Derived Highly Dispersed α-Cobalt Confined in Nitrogen-Doped Carbon Nanofibers Nanozyme for Biomolecule Monitoring, *Anal. Chem.*, 2024, **96**(3), 1345–1353, DOI: 10.1021/acs.analchem.3c05053.

16 R. Liu, *et al.*, Structure Remodeling Strategy for Open-Cage NiFe@Fe-bis-PBA with Enhanced Peroxidase-like Activity To Monitor Tumor Markers, *Anal. Chem.*, 2024, **96**(38), 15338–15346, DOI: 10.1021/acs.analchem.4c02995.

17 R. Liu, *et al.*, Universal MOF nanozyme-induced catalytic amplification strategy for label-free electrochemical immunoassay, *Chin. Chem. Lett.*, 2024, **35**(11), 109664, DOI: 10.1016/j.cclet.2024.109664.

18 J. Du, *et al.*, Metal-organic framework-based biosensing platforms for diagnosis of bacteria-induced infectious diseases, *TrAC, Trends Anal. Chem.*, 2024, **175**, 117707, DOI: 10.1016/j.trac.2024.117707.

19 A. T. E. Vilian, S.-M. Chen, M. A. Ali and F. M. A. Al-Hemaid, Direct electrochemistry of glucose oxidase immobilized on ZrO 2 nanoparticles-decorated reduced graphene oxide

sheets for a glucose biosensor, *RSC Adv.*, 2014, **4**(57), 30358–30367.

20 E. Fazio, *et al.*, Metal-Oxide Based Nanomaterials: Synthesis, Characterization and Their Applications in Electrical and Electrochemical Sensors, *Sensors*, 2021, **21**(7), 2494, DOI: 10.3390/s21072494.

21 A. T. E. Vilian, *et al.*, Hexagonal Co 3 O 4 anchored reduced graphene oxide sheets for high-performance supercapacitors and non-enzymatic glucose sensing, *J. Mater. Chem. A*, 2018, **6**(29), 14367–14379.

22 A. Thakur and A. Kumar, Recent advances on rapid detection and remediation of environmental pollutants utilizing nanomaterials-based (bio)sensors, *Sci. Total Environ.*, 2022, **834**, 155219, DOI: 10.1016/j.scitotenv.2022.155219.

23 S. Sathiyavimal, *et al.*, Green chemistry route of biosynthesized copper oxide nanoparticles using Psidium guajava leaf extract and their antibacterial activity and effective removal of industrial dyes, *J. Environ. Chem. Eng.*, 2021, **9**(2), 105033, DOI: 10.1016/j.jece.2021.105033.

24 E. Rahmati and Z. Rafiee, Synthesis of Co-MOF/COF nanocomposite: application as a powerful and recoverable catalyst in the Knoevenagel reaction, *J. Porous Mater.*, 2021, **28**(1), 19–27, DOI: 10.1007/s10934-020-00965-2.

25 A. Abbasi, S. Tarighi and A. Badiei, A three-dimensional highly stable cobalt(II) metal–organic framework based on terephthalic acid: synthesis, crystal structure, thermal and physical properties, *Transit. Met. Chem.*, 2012, **37**(7), 679–685, DOI: 10.1007/s11243-012-9638-8.

26 P. K. Muchinthala and V. Losetty, Role of phytochemical mediated zinc oxide nanoparticles on biomedical and industrial wastewater treatment: a green approach by experimental and molecular docking exploration, *J. Environ. Chem. Eng.*, 2025, **13**(2), 115333, DOI: 10.1016/j.jece.2025.115333.

27 M. Dhanalakshmi and V. Losetty, Bio-fabrication of multifunctional CuO-ZnO nanocomposites for improved biomedical and industrial wastewater purification by experimental and molecular docking computational investigation, *J. Water Process Eng.*, 2025, **70**, 106933, DOI: 10.1016/j.jwpe.2025.106933.

28 E. L. Cuarán-Rosero, J. F. Muñoz-Chilito and J. E. Rodríguez-Páez, Copper oxide nanoparticles (CuO-NPs): synthesis, characterization and evaluating their ability to remove methylene blue from aqueous solutions without UV irradiation and in the absence of H2O2, *Ceram. Int.*, 2024, **50**(12), 21213–21231, DOI: 10.1016/j.ceramint.2024.03.231.

29 M. Meinert and G. Reiss, Electronic structure and optical band gap determination of NiFe2O4, *J. Phys.: Condens. Matter*, 2014, **26**(11), 115503, DOI: 10.1088/0953-8984/26/11/115503.

30 N. T. T. Le, B. T. D. Trinh, D. H. Nguyen, L. D. Tran, C. H. Luu and T. T. Hoang Thi, The Physicochemical and Antifungal Properties of Eco-friendly Silver Nanoparticles Synthesized by Psidium guajava Leaf Extract in the Comparison With Tamarindus indica, *J. Clust. Sci.*, 2021, **32**(3), 601–611, DOI: 10.1007/s10876-020-01823-6.

31 K. M. Racik, A. Manikandan, M. Mahendiran, P. Prabakaran, J. Madhavan and M. V. Antony Raj, Fabrication of manganese oxide decorated copper oxide (MnO2/CuO) nanocomposite electrodes for energy storage supercapacitor devices, *Phys. E*, 2020, **119**, 114033, DOI: 10.1016/j.physe.2020.114033.

32 M. B. Mobarak, M. S. Hossain, F. Chowdhury and S. Ahmed, Synthesis and characterization of CuO nanoparticles utilizing waste fish scale and exploitation of XRD peak profile analysis for approximating the structural parameters, *Arab. J. Chem.*, 2022, **15**(10), 104117, DOI: 10.1016/j.arabjc.2022.104117.

33 S. Roguai and A. Djelloul, A simple synthesis of CuO NPs for photocatalytic applications and theirs structural and optical properties, *J. New Technol. Mater.*, 2021, **11**(2), 53–57.

34 A. Abraham, R. Silviya, R. Patel, N. Patel and R. Fernandes, MOF derived cobalt-phospho-boride for rapid hydrogen generation via NaBH4 hydrolysis, *Int. J. Hydrogen Energy*, 2024, **77**(September), 1245–1253, DOI: 10.1016/j.ijhydene.2024.06.247.

35 A. K. Ipadeola and K. I. Ozoemena, Alkaline water-splitting reactions over Pd/Co-MOF-derived carbon obtained via microwave-assisted synthesis, *RSC Adv.*, 2020, **10**(29), 17359–17368, DOI: 10.1039/d0ra02307h.

36 Y. Hao and A. S. Teja, Continuous hydrothermal crystallization of-Fe2O3 and Co3O4 nanoparticles, *J. Mater. Sci. Res.*, 2003, **18**, 415–422, DOI: 10.1557/JMR.2003.0053.

37 H. N. Jayasimha, K. G. Chandrappa, P. F. Sanaulla and V. G. Dileepkumar, Green synthesis of CuO nanoparticles: a promising material for photocatalysis and electrochemical sensor, *Sens. Int.*, 2024, **5**, 100254, DOI: 10.1016/j.sintl.2023.100254.

38 M. Wang, *et al.*, Unraveling the tunable selectivity on cobalt oxide and metallic cobalt sites for CO2 hydrogenation, *Chem. Eng. J.*, 2022, **446**, 137217, DOI: 10.1016/j.cej.2022.137217.

39 F. A. Adesanya and O. E. Fayemi, Anthracene electrochemical sensor at fMWCNTs/ZnO modified glassy carbon electrode, *Int. J. Electrochem. Sci.*, 2023, **18**(12), 100382, DOI: 10.1016/j.ijoes.2023.100382.

40 G. M. G. da Silva, P. M. Faia, S. R. Mendes and E. S. Araújo, A Review of Impedance Spectroscopy Technique: Applications, Modelling, and Case Study of Relative Humidity Sensors Development, *Appl. Sci.*, 2024, **14**(13), 5754, DOI: 10.3390/app14135754.

41 R. M. Rodrigues, D. A. Thadathil, G. Shanker, U. Sirimahachai, A. Varghese and G. Hegde, Co-electrodeposited Pi-MnO2-rGO as an efficient electrode for the selective oxidation of piperonyl alcohol, *J. Electrochem. Soc.*, 2023, **170**(3), 36501.

42 M. F. Altahan, A. G. Ali, A. A. Hathoot and M. A. Azzem, Modified electrode decorated with silver as a novel non-enzymatic sensor for the determination of ammonium in water, *Sci. Rep.*, 2023, **13**(1), 16861, DOI: 10.1038/s41598-023-43616-7.

43 F. M. Zanotto, R. A. Fernández and S. A. Dassie, Facilitated proton transfer-electron transfer coupled reactions at

thick-film modified electrodes, *Electrochim. Acta*, 2017, **258**, 727–734, DOI: **10.1016/j.electacta.2017.11.119**.

44 J. A. Quezada-Renteria, L. F. Chazaro-Ruiz and J. R. Rangel-Mendez, Poorly conductive electrochemically reduced graphene oxide films modified with alkyne chains to avoid the corrosion-promoting effect of graphene-based materials on carbon steel, *Carbon*, 2020, **167**, 512–522, DOI: **10.1016/j.carbon.2020.05.069**.

45 A. Bathinapatla, S. Kanchi, P. Singh, M. I. Sabela and K. Bisetty, An ultrasensitive performance enhanced novel cytochrome c biosensor for the detection of rebaudioside A, *Biosens. Bioelectron.*, 2016, **77**, 116–123, DOI: **10.1016/j.bios.2015.09.004**.

46 H.-C. Wang and A.-R. Lee, Recent developments in blood glucose sensors, *J. Food Drug Anal.*, 2015, **23**(2), 191–200, DOI: **10.1016/j.jfda.2014.12.001**.

47 H. Lu, T. Yin, F. Luan, Y. Li and W. Qin, Tailoring the surface of a polymeric membrane with a thin-layer Nafion membrane: construction of an anti-surfactant solid-contact ion-selective electrode, *J. Electroanal. Chem.*, 2025, **977**, 118830, DOI: **10.1016/j.jelechem.2024.118830**.

48 M. Manuel and S. Kanchi, Construction of a waste-derived graphite electrode integrated IL/Ni-MOF flowers/Co3O4 NDs for specific enrichment and signal amplification to detect aspartame, *Colloids Surf., A*, 2025, **705**(P1), 135648, DOI: **10.1016/j.colsurfa.2024.135648**.

49 R. Singh and M. Singh, Molecularly imprinted electrochemical sensor for highly selective and sensitive determination of artificial sweetener Acesulfame-K, *Talanta Open*, 2023, **7**, 100194, DOI: **10.1016/j.talo.2023.100194**.

50 O. A. Arodola, S. Kanchi, P. Hloma, K. Bisetty, A. M. Asiri and Inamuddin, An in silico layer-by-layer adsorption study of the interaction between rebaudioside A and the T1R2 human sweet taste receptor: modelling and biosensing perspectives, *Sci. Rep.*, 2020, **10**(1), 18391, DOI: **10.1038/s41598-020-75123-4**.